

Skeleton-Based Action Segmentation with Multi-Stage Spatial-Temporal Graph Convolutional Neural Networks

Benjamin Filtjens, Bart Vanrumste, Peter Slaets

Abstract—The ability to identify and temporally segment fine-grained actions in motion capture sequences is crucial for applications in human movement analysis. Motion capture is typically performed with optical or inertial measurement systems, which encode human movement as a time series of human joint locations and orientations or their higher-order representations. State-of-the-art action segmentation approaches use multiple stages of temporal convolutions. The main idea is to generate an initial prediction with several layers of temporal convolutions and refine these predictions over multiple stages, also with temporal convolutions. Although these approaches capture long-term temporal patterns, the initial predictions do not adequately consider the spatial hierarchy among the human joints. To address this limitation, we present multi-stage spatial-temporal graph convolutional neural networks (MS-GCN). Our framework decouples the architecture of the initial prediction generation stage from the refinement stages. Specifically, we replace the initial stage of temporal convolutions with spatial-temporal graph convolutions, which better exploit the spatial configuration of the joints and their temporal dynamics. Our framework was compared to four strong baselines on five tasks. Experimental results demonstrate that our framework achieves state-of-the-art performance.

Index Terms—activity segmentation, activity detection, dense labelling, freezing of gait, graph convolutional, MS-GCN, multi-stage, spatial-temporal

I. INTRODUCTION

THE automatic identification and localisation of events and actions in long untrimmed motion capture (MoCap) sequences are crucial for various use-cases in human movement analysis. Typically, MoCap is performed with optical or inertial measurement systems, which encode human movement as a time series of human joint locations and orientations or their higher-order representations. The high-dimensional time series registers the articulated motion as a high degree of freedom human skeleton. Given an untrimmed MoCap sequence, we aim to segment every event and action in time. In the literature, this task falls under the domain of skeleton-based action segmentation.

Related to this task is the task of skeleton-based action recognition. Unlike action segmentation, action recognition aims to classify actions from short and well-segmented video

clips. This domain has made tremendous strides due to the availability of low-cost MoCap systems. These systems are driven by pose estimation algorithms, which are a form of optical MoCap that encode human movement as a time series of human joint locations with a single camera [1], [2]. Human actions can then be recognized by appropriately modelling the high dimensional time series. Earlier methods ignored the spatial hierarchy among the joints and modelled human actions by applying high-level temporal models [3]. Later methods explicitly modelled the natural connection between joints [4]. These methods showed encouraging improvement, which suggests the significance of modelling the spatial hierarchy among the joints. State-of-the-art approaches model the skeleton sequences as a spatial-temporal graph [5], [6]. The idea is to construct a graph in which each node corresponds to a human body joint and the edges correspond to the spatial connectivity among the joints and the temporal connectivity of the same joint across time. The spatial-temporal graph can then be modelled by graph neural networks, which generalize convolutional neural networks to graphs of arbitrary structures [7], [8]. However, skeleton-based action segmentation is more challenging than recognition, due to the need for simultaneous recognition and localization. Despite its broad potential in human movement analysis, a proper framework for this task has not yet been established.

Within the generic domain of action segmentation, i.e. approaches that are not specifically designed for skeleton data, earlier methods mainly utilized a sliding-window scheme [9], [10]. However, the optimal window size is often a trade-off between model expressivity, i.e., the models' ability to capture long-term temporal context, and the sensitivity of the model to take into account short actions [11]. Recent methods, such as temporal convolutional neural networks (TCN) [12], can operate on untrimmed sequences and classify each time sample, termed action segmentation, for simultaneous action recognition and localisation. For action segmentation, the predictions tend to vary at a high temporal frequency, often resulting in over-segmentation errors. To address this problem, state of the art approaches include refinement stages [13]. The idea is to employ a temporal model to generate an initial prediction and refine these predictions over multiple stages. However, these generic action segmentation approaches do not consider the spatial hierarchy among the skeleton joints.

We introduce a for an architecture for skeleton-based action segmentation, termed multi-stage spatial-temporal graph convolutional neural network (MS-GCN) [14]. Our architecture

Submitted on x December 2021

Benjamin Filtjens and Peter Slaets are with the Department of Mechanical Engineering, KU Leuven, 3001 Leuven, Belgium. (email: benjamin.filtjens@kuleuven.be and peter.slaets@kuleuven.be).

Benjamin Filtjens and Bart Vanrumste are with the Department of Electrical Engineering (ESAT), KU Leuven, 3001 Leuven, Belgium. (email: benjamin.filtjens@kuleuven.be and bart.vanrumste@kuleuven.be).

combines state-of-the-art practices in skeleton-based action recognition, i.e. spatial-temporal graph convolutional neural networks (ST-GCN) [5], and general action segmentation, i.e. multi-stage temporal convolutional neural networks (MS-TCN) [13]. First, we extend ST-GCN for action segmentation by including dilation on the temporal graph to increase the temporal receptive field [15]. Next, we modify MS-TCN by decoupling the prediction generation stage from the refinement stages, allowing us to address the different goals of these stages. Specifically, we replace the TCN-based temporal layers that generate an initial prediction by the ST-GCN layers to appropriately model the spatial hierarchy among the joints. As skeleton-based action segmentation is a young domain, we introduce five relevant use-cases from public and proprietary datasets. Our framework was compared to four strong deep learning baselines.

II. SKELETON-BASED ACTION SEGMENTATION

This section first introduces the problem of skeleton-based action segmentation. Next, we introduce the building blocks of our generic framework. The aim of our framework is to amalgamate the best practices in convolutional network design into a simple baseline architecture for skeleton-based action segmentation. The architecture is termed multi-stage spatial-temporal graph convolutional neural network (MS-GCN), as it combines the best practices from spatial-temporal graph convolutional neural networks (ST-GCN) [5] and multi-stage temporal convolutional neural networks (MS-TCN) [13]. The distinguishing characteristics of the MS-GCN architecture are: (1) dilated temporal convolutions to learn long-term temporal patterns, (2) spatial graph convolutions to learn spatial patterns, (3) multiple stages of refinement to reduce the number of segmentation errors. These characteristics are further discussed within this section.

A. Problem statement

The aim of the generic architecture is to learn a statistical model $z : x \rightarrow \hat{y}$ that transforms an input MoCap sequence $X = x_0, \dots, x_T$ into a predicted output sequence $\hat{Y} = \hat{y}_0, \dots, \hat{y}_T$. The MoCap representation or feature map can be generically represented as: $f \in \mathbb{R}^{T \times N \times C}$, where T are the number of samples, N are the number of nodes, and C are the number of feature channels per node. The predicted output sequence can be defined as: $\hat{Y} \in \mathbb{R}^{T \times l}$, where $\hat{y}_{t,l}$ is the probability of class l at sample t . We focus on post hoc (acausal) movement analysis. Thus, the prediction for sample \hat{y}_t may depend on future inputs $f_{in_{t+1}}, \dots, f_{in_T}$.

B. Dilated temporal convolution

Convolutional neural networks (CNN) are ideal for processing data with a grid-like topology such as time-series (1D CNN) and images (2D CNN) [16]. A CNN learns an expressive representation through altering convolutional and pooling layers [17]. The pooling layers downsample the temporal representation, allowing the model to capture long-range dependencies at the cost of losing fine-grained information.

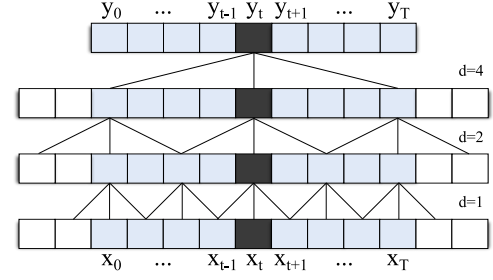


Fig. 1. Visual overview of a (dilated) temporal convolutional neural network (TCN). The visualized network is implemented in acausal mode, since the filters take into account future observations x_{t+1}, \dots, x_T . The first layer has a dilation rate of 1, reducing this layer to a regular convolution. By increasing the dilation factor throughout the network, the deeper layers can represent a wider range of inputs, thereby expanding the temporal receptive field of the network.

Recent temporal convolutional neural networks (TCN) omit pooling and instead use dilated convolutions [15] to capture long-range dependencies while keeping the temporal representation intact [13]. For an input feature map f_{in} and a filter p , the dilated convolution on sample t of the feature map is defined as [18]:

$$(f_{in} *_d p)(t) = \sum_{i=0}^{k-1} p(i) \cdot f_{in_{t-d \cdot i}}, \quad (1)$$

where $*_d$ is the dilated convolution operator with dilation rate d , k is the size of the filter (kernel), and $t - d \cdot i$ is used to indicate that the filter in Equation 1 is applied in acausal mode, i.e. direction of the past. The filter can be implemented in acausal mode by zero-padding symmetrically, as visualized in Figure 1.

C. Graph convolution

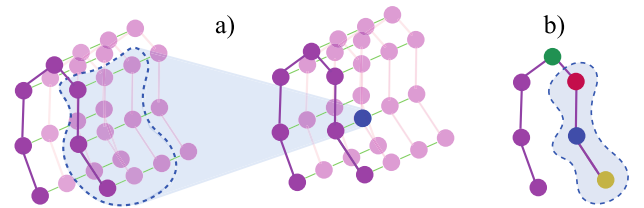


Fig. 2. Visual overview of a spatial-temporal graph (a) and spatial partitioning strategy (b).

Graph convolutional neural networks (GCNs) generalize CNNs to non-euclidian structured data [8]. Yan et al. extended GCNs to exploit the inherent spatial relationship among the joints of a skeleton [5]. Their approach termed spatial-temporal graph convolutional networks (ST-GCN) learns a representation on a graph $G = (V, E, A)$ which takes as input:

- A set of nodes $V = \{v_{ti} | t = 1, \dots, T, i = 1, \dots, N\}$ for a skeleton sequence of N joints and T samples.
- Two sets of edges $E_S = \{v_{ti}v_{tj} | (i, j) \in H\}$ and $E_F = \{v_{ti}v_{(t+1)i}\}$, where H is the set of connected joints. E_S refers to the intra-skeleton edges at each frame (spatial dimension), and E_F refers to the inter-frame

connection of the same joints over all of the frames (temporal dimension).

- A description of the graph structure in the form of an adjacency matrix A .

For instance, Figure 2(a) visualizes the spatial-temporal graph. The joints represent the nodes of the graph (purple nodes), their natural connections are the spatial edges (purple lines), and the connection between adjacent frames are the temporal edges (green lines).

In the spatial dimension, the graph convolution operation on node v_{ti} is defined as [5]:

$$f_{gcn}(v_{ti}) = \sum_{v_{tj} \in B(v_{ti})} \frac{1}{Z_{ti}(v_{tj})} f_{in}(v_{tj}) \cdot w(l_{ti}(v_{tj})), \quad (2)$$

where f_{in} and f_{gcn} denote the input feature map and output feature map, respectively. The term $B(v_{ti})$ denotes the sampling area of node v_{ti} , with the nodes within the sampling area denoted as v_{tj} . A mapping function l_{ti} is defined to map each node with a unique weight vector w . Figure 2(b) visualizes this strategy for a single frame t , where the kernel size is set as 3 and the sampling area B is partitioned into 3 subsets based on a nodes distance with respect to a self-selected root node (green). The three subsets in this partitioning strategy are the node itself (blue), the node closer to the root node (red), and the node further from the root node (yellow). The normalizing term Z_{ij} is added to balance the contributions of different subsets to the output.

D. Refinement stages

As predictions are made at high temporal frequencies, over-segmentation errors, i.e. an action is segmented into multiple shorter actions, often occur. A common strategy to alleviate this problem in pixel-wise labelling of images is to generate an initial prediction, then refine this initial prediction using the interactions between neighbouring pixels [16]. Farha and Gall extend this to action segmentation in time series data [13]. The idea is to stack several predictors that each operates directly on the output of the previous one to incrementally refine the predictions. As the predictors are typical TCNs, this architecture is termed multi-stage temporal convolutional neural network (MS-TCN).

III. DEEP LEARNING MODELS

The previous section introduced the three building blocks that characterizes the MS-GCN architecture. As the MS-GCN architecture combines the best practices from MS-TCN and ST-GCN, we include these as a baseline. We additionally include a bidirectional long short term memory-based network (LSTM) [19], and temporal convolutional neural network-based network (TCN) [12], as they are often considered an important baseline in action segmentation of MoCap data [20]–[22].

The implementation details of the employed models are visualized in Figure 3. The first layer of all models is a batch normalization (BN) layer that normalizes the inputs and accelerates training [23]. After normalization, the input is reshaped into the accepted formats of the specified models.

For the graph-based models, i.e. ST-GCN and MS-GCN, the data is shaped into $T \times C_{in} \times N$, where N represents the number of nodes, C_{in} the number of input channels, and T the number of samples. For the temporal models, i.e. LSTM, TCN, and MS-TCN, the data is shaped into $T \times C_{in} * N$. For these models, the spatial feature dimension is thus collapsed.

A. LSTM

The first layer of our recurrent model is an LSTM layer, which computes the following function:

$$\begin{aligned} i_t &= \sigma(f_{in_t} W_{ii} + b_{ii} + h_{t-1} W_{hi} + b_{hi}), \\ j_t &= \sigma(f_{in_t} W_{if} + b_{if} + h_{t-1} W_{hf} + b_{hf}), \\ g_t &= \tanh(f_{in_t} W_{ig} + b_{ig} + h_{t-1} W_{hg} + b_{hg}), \\ o_t &= \sigma(f_{in_t} W_{io} + b_{io} + h_{t-1} W_{ho} + b_{ho}), \\ c_t &= j_t \odot c_{t-1} + i_t \odot g_t, \\ h_t &= \tanh(c_t) \odot o_t, \end{aligned}$$

where h_t is the hidden state at time t , c_t is the cell state at time t , f_{in_t} is the input feature map at time t , h_{t-1} is the hidden state of the layer at time $t-1$. The terms i_t , j_t , g_t , and o_t are the input, forget, cell, and output gates, respectively. The terms σ , \tanh , and \odot are the sigmoid function, hyperbolic tangent function, and Hadamard product, respectively. The weight matrices are represented by W , with subscripts representing from-to relationships. The LSTM layer above is causal, as the hidden state h_t depends only on x_0, \dots, x_t . For our recurrent model, the LSTM was implemented in acausal mode, i.e. take into account future observations x_{t+1}, \dots, x_T , by training it in the positive and negative time direction (bidirectional) [19], [24].

B. TCN

The first layer of the TCN-based model is a 1×1 convolutional layer that adjusts the input dimension C_{in} to the number of filters C in the network, formalized as:

$$f_{adj} = W_1 f_{in} + b, \quad (3)$$

where $f_{adj} \in \mathbb{R}^{T \times C}$ is the adjusted feature map, $f_{in} \in \mathbb{R}^{T \times C_{in}}$ the input MoCap sequence, $b \in \mathbb{R}^C$ the bias term, and $W_1 \in \mathbb{R}^{1 \times C_{in} \times C}$ the weights of the 1×1 convolution filter with C_{in} input feature channels and C equal to the number of feature channels in the network.

The adjusted input is passed through several TCN blocks. Each TCN block applies a dilated temporal convolution [15], BN, ReLU non-linear activation, and a residual connection between the activation map and the input. Formally, this process is defined as:

$$f_{out} = \delta(BN(W f_{adj} + b)) + f_{adj}, \quad (4)$$

where $f_{out} \in \mathbb{R}^{T \times C}$ is the output feature map, $b \in \mathbb{R}^C$ the bias term, $W \in \mathbb{R}^{k \times C \times C}$ the weights of the dilated convolution filter with kernel size k , and δ the ReLU function.

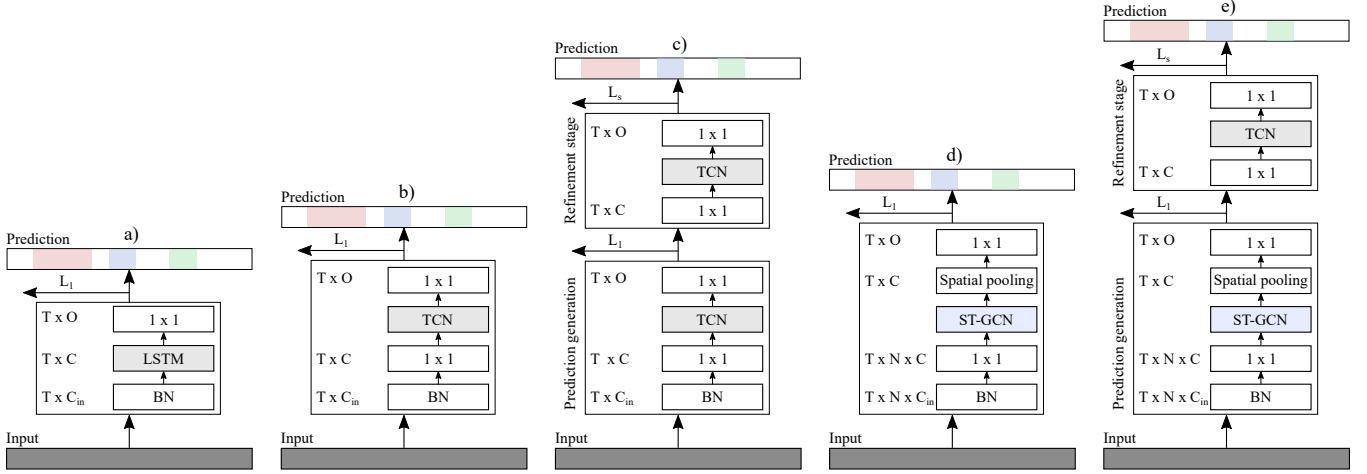


Fig. 3. Overview of the MS-GCN and the four baseline deep learning models. The models take as input a MoCap sequence and generate as output a sequence of actions. The five deep learning models are: (1) a long short-term memory network (LSTM), (b) a temporal convolutional neural network (TCN), (c) a multi-stage temporal convolutional neural network (MS-TCN), (d) a spatial-temporal graph convolutional neural network (ST-GCN), and (e) a multi-stage spatial-temporal graph convolutional neural network (MS-GCN). The terms BN and L_s denote the batch normalization layer and the loss of stage s , respectively.

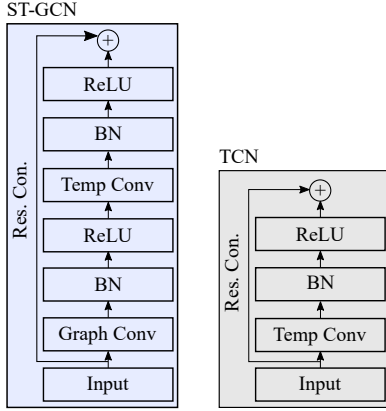


Fig. 4. Visual overview of a temporal convolutional (TCN) and spatial-temporal graph convolutional (ST-GCN) block [5]. ST-GCN generates a spatial-temporal feature map by applying a spatial graph convolution and a temporal convolution, both of which are followed by batch normalization (BN) and a ReLU non-linearity. Moreover, a residual connection is added to each block.

C. ST-GCN

The first layer of the ST-GCN-based model is a 1×1 convolutional layer that adjusts the input dimension C_{in} to the number of filters C in the network, formalized as:

$$f_{adj} = W_1 f_{in} + b, \quad (5)$$

where $f_{adj} \in \mathbb{R}^{T \times N \times C}$ is the adjusted feature map, $f_{in} \in \mathbb{R}^{T \times N \times C_{in}}$ the input MoCap sequence, $b \in \mathbb{R}^C$ the bias term, $W_1 \in \mathbb{R}^{1 \times 1 \times C_{in} \times C}$ the weights of the 1×1 convolution filter with C_{in} input feature channels and C equal to the number of feature channels in the network.

The adjusted input is passed through several ST-GCN blocks [5]. Each ST-GCN first applies a graph convolution, transforming Equation 2 into:

$$f_{gcn} = \sum_p A_p f_{adj} W_p M_p, \quad (6)$$

where $f_{adj} \in \mathbb{R}^{T \times N \times C}$ is the adjusted input feature map, $f_{gcn} \in \mathbb{R}^{T \times N \times C}$ the output feature map of the spatial graph convolution, and W_p the $1 \times 1 \times C \times C$ weight matrix. The matrix $A_p \in \{0, 1\}^{N \times N}$ is the adjacency matrix, which represents the spatial connection between the joints. The adjacency matrix $A_p = D_p^{-\frac{1}{2}} A_p D_p^{-\frac{1}{2}}$, where D_p is the diagonal node degree matrix. Multiplying $D_p^{-\frac{1}{2}} A_p D_p^{-\frac{1}{2}}$ corresponds to symmetrically normalizing A , which prevents changing the scale of the features based on the number of connections [8]. The graph is partitioned into three subsets based on the spatial partitioning strategy, as was visualized in Figure 2(b) [5]. There are thus three different weight vectors W_p that allow modelling of relative properties between the nodes. The matrix M_p is a learnable $N \times N$ attention mask that indicates the importance of each node and its spatial partitions.

Next, after passing through a BN layer and ReLU non-linearity, the ST-GCN block performs a dilated temporal convolution. The dilated temporal convolution is, in turn, passed through a BN layer and ReLU non-linearity, and lastly, a residual connection is added between the activation map and the input. This process is formalized as:

$$f_{out} = \delta(BN(W f_{gcn} + b)) + f_{adj}, \quad (7)$$

where $f_{out} \in \mathbb{R}^{T \times N \times C}$ is the output feature map, $b \in \mathbb{R}^C$ the bias term, $W \in \mathbb{R}^{k \times 1 \times C \times C}$ the weights of the dilated convolution filter with kernel size k . The output feature map is passed through a spatial pooling layer that aggregates the spatial features among the N joints.

D. Sample-based prediction

The three single-stage models map an input sequence X to a hidden representation $f_{out} \in \mathbb{R}^{T \times C}$, with C determined by the number of convolutional filters (ST-GCN and TCN) or the number of hidden units (LSTM), and length T the same as the input sequence. The hidden representation of each model is passed through a 1×1 convolution and a softmax activation

function to get the probabilities for the l output classes for each sample in-time, formalized as:

$$\hat{y}_t = \zeta(W_1 f_{out} + b), \quad (8)$$

where \hat{y}_t are the class probabilities at time t , f_{out} the output of the single stage models at time t , $b \in \mathbb{R}^l$ the bias term, ζ the softmax function, $W_1 \in \mathbb{R}^{1 \times C \times l}$ the weights of the 1×1 convolution filter with C input channels and l output classes.

E. MS-TCN

The MS-TCN-based model first features a prediction generation stage of several TCN blocks, as explained in Chapter III-B, which generates an initial prediction $\hat{Y} \in \mathbb{R}^{T \times l}$. Next, the prediction is passed through several refinement stages. Each refinement stage contains several TCN blocks, and each stage operates directly on the softmax activations of the previous stage. Formally, this process is defined as:

$$\hat{Y}^s = \Gamma(\hat{Y}^{s-1}), \quad (9)$$

where $\hat{Y}^s \in \mathbb{R}^{T \times l}$ is the output at stage s , \hat{Y}^{s-1} the output of the previous stage, and Γ the single-stage TCN, as explained in section III-B.

F. MS-GCN

The multi-stage graph convolutional neural network (MS-GCN) [14], generalizes the multi-stage temporal convolutional neural network (MS-TCN) [13] to graph-based data. Formally, the MS-TCN and MS-GCN architectures are composed of multiple stages of temporal 1D convolutions, where each stage refines the predictions of the previous stage. Unlike the MS-TCN, the MS-GCN replaces the initial stage of 1D convolutional layers with multiple layers of spatial-temporal graph convolutional layers (ST-GCN) [5].

The proposed MS-GCN model first features a prediction generation stage of several ST-GCN blocks, as explained in Chapter III-C, which generates an initial prediction $\hat{Y} \in \mathbb{R}^{T \times l}$. Next, the prediction is passed through several refinement stages. Each refinement stage contains several TCN blocks, and each stage operates directly on the softmax activations of the previous stage. Formally, this process is defined as:

$$\hat{Y}^s = \Gamma(\hat{Y}^{s-1}), \quad (10)$$

where $\hat{Y}^s \in \mathbb{R}^{T \times l}$ is the output at stage s , \hat{Y}^{s-1} the output of the previous stage, and Γ the single-stage TCN, as explained in section III-B.

G. Implementation details

The models were trained by minimizing a combined cross-entropy (CE) and mean squared error (MSE) loss. The CE loss was defined as:

$$\mathcal{L} = \sum_{s=1}^S \mathcal{L}_{s,cls}, \quad (11)$$

$$\mathcal{L}_{cls} = \frac{1}{T} \sum_t -y_{t,l} \log(\hat{y}_{t,l}), \quad (12)$$

where \mathcal{L} is the total loss over all S stages and \mathcal{L}_{cls} the CE loss with $y_{t,l}$ and $\hat{y}_{t,l}$ the ground truth label and predicted probability for class l at time t , respectively. The combined CE and MSE loss was defined as [13]:

$$\mathcal{L} = \sum_{s=1}^S \mathcal{L}_{s,cls} + \lambda \mathcal{L}_{s,T-MSE}, \quad (13)$$

where \mathcal{L}_{T-MSE} is the MSE loss and λ is a hyperparameter that determines its contribution. The combined loss was proposed by Farha and Gall to avoid over-segmentation errors [13], which occur when predictions vary at an unrealistically high sample frequency. The MSE term negates this effect by calculating the truncated mean squared error over the sample-wise log probabilities. The MSE loss function is defined as:

$$\mathcal{L}_{T-MSE} = \frac{1}{TL} \sum_{t,l} \tilde{\Delta}_{t,l}^2, \quad (14)$$

$$\tilde{\Delta}_{t,l} = \begin{cases} \Delta_{t,l} & : \Delta_{t,l} \leq \tau \\ \tau & : otherwise \end{cases}, \quad (15)$$

$$\Delta_{t,l} = |\log(\hat{y}_{t,l}) - \log(\hat{y}_{t-1,l})|, \quad (16)$$

where T is the sequence length, L is the number of classes, and $\hat{y}_{t,l}$ is the probability of class l at time t . The hyperparameter τ defines the threshold to truncate the smoothing loss.

To avoid model selection bias for the convolutional models, i.e. TCN, ST-GCN, MS-TCN, and MS-GCN, the same model hyperparameters were chosen as MS-TCN [13]. More specifically, each layer had 64 filters with a temporal kernel size of 3. All multi-stage models had 1 prediction generation stage and 3 refinement stages, and each stage had 10 layers. The convolutions were acausal, i.e. they could take into account both past and future input features. The dilation factor of the temporal convolutions doubled at each layer, i.e. 1, 2, 4, ..., 512.

For the recurrent model, we followed a configuration that is conventional in MoCap-based action segmentation. For instance, prior work in gait cycle and FOG subtask segmentation used recurrent models of 1-3 LSTM layers of 32 - 128 cells each [21], [25]. For our recurrent model, we used two forward LSTM layers and two backward LSTM layers, each with 64 cells.

The optimizer and loss hyperparameters were also selected according to MS-TCN [13]. For the loss, we set $\tau = 4$ and $\lambda = 0.15$. For the optimizer, we used Adam with a learning rate of 0.0005 [26]. All models were trained for 100 epochs with a batch size of 8.

IV. EVALUATION

We present five datasets for skeleton-based action segmentation. Three of the five datasets are for action segmentation, with each featuring a different MoCap representation, i.e., inertial-based (HuGaDB), markerless optical MoCap (PKU-MMDv2), and marker-based optical MoCap (LARA). Two of the five datasets involve typical segmentation tasks commonly used in clinical gait analysis. For these two tasks, additional context regarding the relevance is provided.

A. Peking University - Continuous Multi-Modal Human Action Understanding (PKU-MMD v2)

PKU-MMD is a benchmark dataset for continuous 3D human action understanding [27]. In this study, we use the smaller phase 2 partition of the dataset. This dataset contains 2000 short video sequences in 49 action categories, performed by 13 subjects in three camera views. MoCap was performed with a Kinect v2 optical marker-less motion capture system at 30 Hz. The Kinect system records the 3-axis locations of 25 major body joints.

B. Human Gait Database (HuGaDB)

HuGaDB is an action segmentation dataset where a total of 18 subjects carried out typical lower limb activities, e.g. walking, running, and cycling [28]. MoCap was performed with 6 inertial measurement units (IMUs) at a sampling frequency of 60 Hz. The IMUs were placed on the right and left thighs, shins and feet.

C. Logistic Activity Recognition Challenge (LARA)

LARA is a recently released dataset of subjects carrying out typical warehousing activities [29]. Fourteen subjects carried out a total of eight actions. MoCap was performed by an optical MoCap system that recorded the motion of 39 reflective markers at a sampling frequency of 200 Hz. All subjects participated in a total of 30 recordings of 2 minutes each. The actions were performed under three different warehousing scenarios that each aimed to mimic real-world warehousing activities. In scenario 1, subjects 1 to 6 performed 30 recordings, and subjects 7 to 14 performed 2 recordings. Subjects 7 to 14 additionally performed 14 recordings in scenarios 2 and 3. The authors proposed to tackle the automated skeleton-based segmentation task with a TCN-based model that classified temporal segments extracted by a sliding window.

D. Gait phase and freezing of gait segmentation (FOG-GAIT)

Freezing of gait (FOG) and temporal gait disturbances in people with Parkinson's disease (PwPD) are commonly assessed during complex experimental protocols that involve turning with or without a cognitive dual-task [30], [31], which serve as triggers to elicit FOG [32]. The current assessment implies that the gait cycle phases, i.e. double support 1, single support, double support 2, and swing, and the FOG episodes are annotated manually based on the 3D marker trajectories of a motion capture system, and standard camera footage [31], [33]. These time-consuming tasks motivate the search for algorithms to automatically delineate the gait cycle phases and FOG episodes. State-of-the-art deep learning models tackle the gait segmentation task with TCN or LSTM-based models [20], [25].

A proprietary MoCap dataset of seven PwPD and FOG that froze during the protocol was used [30]. The subjects were instructed to complete a standardized protocol consisting of straight-ahead walking, 180 degree turning, and 360 degree turning. The experiments were offered randomly and performed with our without a cognitive dual-task [34]. Two

optical markers were placed at a .5m distance from each other on the floor to standardize the turning radius. The data acquisition was further standardized by defining a zone of one meter before and after the turn in which MoCap data was stored. The FOG events and gait cycle phases were visually annotated by an experienced clinical operator. MoCap was performed at a sampling frequency of 100 Hz with a ten camera Vicon motion capture system. Optical markers were placed according to the plugin-gait configuration [35].

E. Timed Up-and-Go (TUG) sub-task segmentation

The timed up-and-go (TUG) is a commonly used test in clinical practice to evaluate a subjects' functional mobility [36]. During the TUG, subjects carry out several sub-activities that are common in daily life, i.e. sitting, standing up, walking, turning around, walking back, and sitting back down. In clinical practice, the timing of the sub-activities is commonly assessed under clinical supervision. Therefore, there is increased interest in automatic TUG analysis and sub-activity segmentation techniques. State-of-the-art deep learning models tackle this task with LSTM-based models [37].

We used a public dataset that aims to recruit a total of 500 healthy participants (aged 21-80) of Asian ethnicity [38]. At the time of this study, the data of only 10 participants were available. Each participant carried out the TUG 3 times, resulting in a total of 30 recordings. Motion capture was performed with a Qualisys optical motion capture system that recorded the motion of reflective markers at a sampling rate of 200 Hz. The markers were placed according to the modified Calibrated Anatomical System Technique (CAST) [39]. The TUG sub-activities were visually annotated by an experienced clinical operator.

F. Graph representations

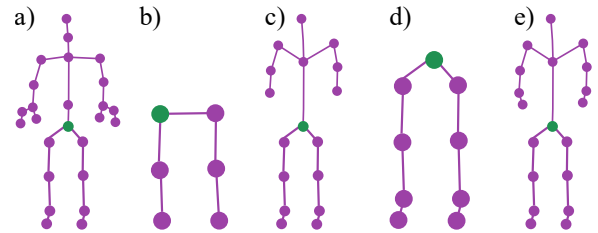


Fig. 5. Different graph representations for (a) PKU-MMD v2, (b) HuGaDB, (c) LARA, (d) FOG-GAIT, (e) TUG. The purple dots represent the nodes of the graph, the purple lines the spatial edges (excluding self-connections), and the green dot the root node.

For the graph-based models, i.e. ST-GCN and MS-GCN, the data is shaped into $T \times C_{in} \times N$, where N represents the number of nodes, C_{in} the number of input channels, and T the number of samples. The $N \times N$ adjacency matrix and input channels C_{in} differ across datasets. For each dataset, the skeleton graphs are visualized in Figure 5. For HuGaDB we used the 3-axis accelerometer and 3-axis gyroscope data, for LARA the 3-axis limb position and orientation, and for PKU-MMD v2, TUG, and FOG-GAIT we computed the 3-axis displacement and 3-axis relative coordinates (with respect to the root node Figure 5) from the 3D joint positions.

G. Metrics

TABLE I
DATASET CHARACTERISTICS.

Task	Partitions	Sample rate	#Nodes
PKU-MMD v2	3/10	30 Hz	25
HuGaDB	4/18	60 Hz	6
LARa	4/14	50 Hz	17
FOG-GAIT	LOSO	50 Hz	9
TUG	LOSO	50 Hz	19

Overview of the partitioning, sample rates, and number of nodes across datasets. For the fixed test/train partition of HuGaDB, we selected the first subjects as test subjects, i.e. subjects 1-4 for HuGaDB. For the fixed test/train partition of PKU-MMD v2, the 4 test subjects were provided by the authors of the dataset. For LARa, S1-6 and S7-14 perform different experiments. To cover both experiments, we take subjects 5-8 for our test partition.

All approaches generate a prediction $\hat{Y} = \hat{y}_{0,l}, \dots, \hat{y}_{T,l}$, where $\hat{y}_{t,l}$ is the probability of class l at sample t . We follow convention by quantitatively evaluating the predictions with respect to the ground truth annotations by means of a sample-wise and a segment-wise evaluation metric.

For the segment-wise metric, we use the F1@50 as proposed by Lea et al. [12]. to compute the segmental metric, a predicted action segment is first classified as a true positive (TP) or false positive (FP) by comparing its intersection over union (IoU) with respect to the corresponding expert annotation. If the IoU crosses a predetermined overlap threshold it is classified as a true positive segment (TP), if it does not, as a false positive segment (FP). The number of false-negative segments (FN) in a trial is calculated by subtracting the number of correctly predicted segments from the number of segments that the experts had demarcated. From the classified segments, the segmental F1-score for each action can be computed as:

$$F1@_{\tau} = \frac{TP}{TP + \frac{1}{2}(FP + FN)}, \quad (17)$$

where τ denotes the IoU overlap.

For the sample-wise metric, we report the accuracy. The term sample-wise denotes that the metric is computed for each sample or timestep. Unlike the segment-wise metric, the sample-wise accuracy does not heavily penalize over-segmentation errors. Reporting both the sample-wise accuracy and the segment-wise F1@50 thus allows assessment of over-segmentation problems. The sample-wise accuracy is simply computed as the number of correctly classified samples divided by the total number of samples.

All use cases were evaluated by assessing the generalization of the models to previously unseen subjects. For the three larger action segmentation datasets, we used a fixed test/train partition. For the two smaller gait analysis datasets, we used a leave one subject out (LOSO) cross-validation approach. The three high sample rate marker-based MoCap datasets were resampled to 50 Hz. No additional pre-processing was performed. A summary is provided in Table I.

H. Statistics

We aim to determine if the differences in predictive performance between the five DL architectures is statistically

TABLE II
ACTION SEGMENTATION RESULTS.

PKU-MMD v2	F1@50	Acc
Bi-LSTM	22.7	59.6
TCN	13.8	61.9
ST-GCN	15.5	64.9
MS-TCN	46.3	65.5
MS-GCN	51.6	68.5
HuGaDB	F1@50	Acc
Bi-LSTM	81.5	86.1
TCN	56.8	88.3
ST-GCN	67.7	88.7
MS-TCN	89.9	86.8
MS-GCN	93.0	90.4
LARa	F1@50	Acc
Bi-LSTM	32.3	63.9
TCN	20.0	61.5
ST-GCN	25.8	67.9
MS-TCN	39.6	65.8
MS-GCN	43.6	65.6
FOG-GAIT	F1@50	Acc
Bi-LSTM	92.1	90.6
TCN	89.9	89.8
ST-GCN	90.8	89.4
MS-TCN	92.5	86.7
MS-GCN	95.0	90.1
TUG	F1@50	Acc
Bi-LSTM	97.1	93.2
TCN	84.4	92.7
ST-GCN	93.8	93.2
MS-TCN	96.5	92.7
MS-GCN	97.9	93.6

Skeleton-based action segmentation results on PKU-MMD v2, HuGaDB, LARa, FOG-GAIT, and TUG. All results are quantified in terms of segment-wise F1@50 and sample-wise accuracy (Acc).

significant. Several statistical methods have been proposed to compare machine learning algorithms [40], [41]. Demšar and Garcia et al. recommend the non-parametric Friedman test [42], with the corresponding post-hoc tests, for the comparison of more than two classifiers over multiple datasets or trials. We used Friedman's test to evaluate the null hypothesis that there is no difference in the classification performance of the five DL architectures on a particular dataset. The post-hoc tests were used to evaluate the null hypothesis that there is no difference in the classification performance between the proposed MS-GCN model and the four baselines on a particular dataset. The post-hoc hypotheses were corrected for multiple comparisons, as defined in Li [37].

All statistical analyses were performed using the scmamp package, version 0.2.55 [43], within The R programming language, version 4.0.3 [44]. The scmamp package implemented Friedman's test according to the version by Demšar [40] and the post-hoc tests according to the version by Garcia et al. [41].

V. RESULTS

Results on all five datasets in terms of the segment-wise F1@50 and sample-wise accuracy (Acc) are shown in Table II. Figure 6 gives a visual overview of the segmentation results for MS-GCN. Sample-wise accuracy and segment-wise F1@50

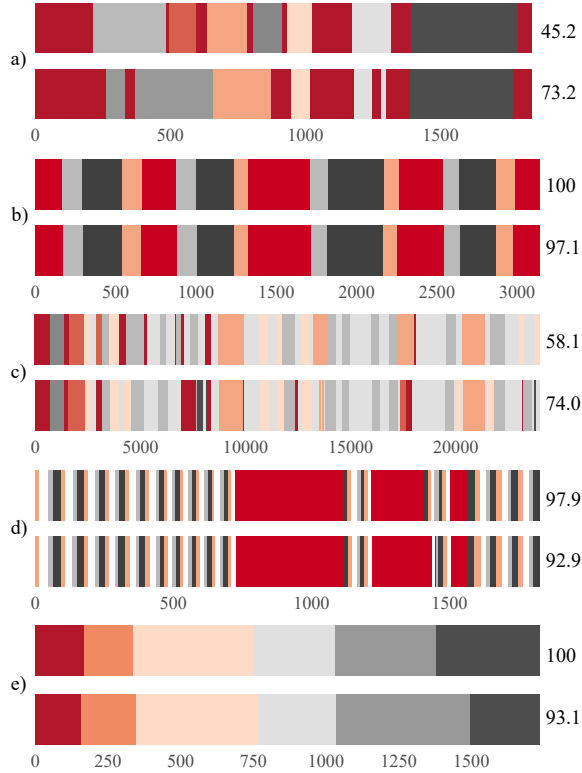


Fig. 6. Visual overview of action segmentation results for one sequence of each use-case. From top to bottom: (a) PKU-MMD v2, (b) HuGaDB, (c) LARa, (d) FOG-GAIT, and (e) TUG. For each use-case, the first sequence represents the GT and the second the segmentation by MS-GCN. For the visualized sequences, the segment-wise F1@50 score is given after the GT sequence and the sample-wise accuracy after the predicted sequence.

for each sequence are included for comparison. The results of the statistical hypotheses tests and the spread across evaluation trials are visualized in Figure 7. All methods were evaluated in acausal mode.

Notice that ST-GCN and MS-GCN, and TCN and MS-TCN achieve similar sample-wise accuracy but very different F1@50 scores. The statistical tests confirm these observations, as the difference in F1@50 between ST-GCN and MS-GCN was statistically significant at the 95% level across all datasets except for the TUG dataset, while the difference in sample-wise accuracy varied with MS-GCN performing significantly better (PKU-MMD and FOG-GAIT), no significant effect (HuGaDB and TUG), and ST-GCN performing significantly better (LARa). Thus, the refinements significantly reduce the number of segmentation errors.

Also, notice that the ST-GCN and MS-GCN pair outperform the TCN and MS-TCN pair across all tasks. This effect was found to have a higher impact on the sample-wise accuracy than on the number of segmentation errors (F1@50). The statistical tests confirm these observations, as the difference between MS-GCN and MS-TCN was statistically significant at the 95% level on two datasets (PKU-MMD and FOG-GAIT) for the F1@50 and on three datasets (PKU-MMD, HuGaDB, and FOG-GAIT) for the sample-wise accuracy. Thus, it is beneficial to explicitly model the spatial hierarchy among the joints or limbs for these use-cases.

A. Ablative experiments

Ablative experiments for MS-GCN were carried out to assess the effect of the introduced dilated convolutions in the prediction generation stage. The experiments were carried out on PKU-MMD v2, HuGaDB, and LARa. Compared to the results in Table II, it is evident that the introduced dilation within the ST-GCN layers of the prediction generation stage has a positive effect on both metrics across the three datasets.

TABLE III
ABLATIVE EXPERIMENT: ASSESSING THE EFFECT OF DILATION IN THE PREDICTION GENERATION STAGE.

Dataset	F1@50	Acc
PKU-MMD v2	44.8	68.4
HuGaDB	75.5	83.8
LARa	37.5	57.0

VI. CONCLUSION

This paper introduced a framework for skeleton-based action segmentation, termed multi-stage spatial-temporal graph convolutional network (MS-GCN). We presented five challenging use-cases of skeleton-based action segmentation in human action understanding and clinical gait analysis. The results indicated that our framework statistically outperformed four strong baselines on four of the five datasets. For the fifth dataset, i.e. the segmentation of TUG sub-activities, the task was found to be too simple, resulting in minimal to no statistical effect in the predictive performance of the models. In conclusion, we believe that the MS-GCN framework, initially developed for FOG segmentation, is a formidable baseline for skeleton-based action segmentation tasks. Our framework is available at <https://github.com/BenjaminFiltjens/MS-GCN>.

REFERENCES

- [1] J. Shotton, R. Girshick, A. Fitzgibbon, T. Sharp, M. Cook, M. Finocchio, R. Moore, P. Kohli, A. Criminisi, A. Kipman, and A. Blake, "Efficient human pose estimation from single depth images," *IEEE Trans. Pattern Anal. Mach. Intell.*, vol. 35, no. 12, pp. 2821–2840, Dec. 2013.
- [2] Z. Cao, G. Hidalgo, T. Simon, S. E. Wei, and Y. Sheikh, "Openpose: Realtime multi-person 2d pose estimation using part affinity fields," *IEEE Transactions on Pattern Analysis and Machine Intelligence*, vol. 43, no. 1, pp. 172–186, 2021.
- [3] B. Fernando, E. Gavves, M. José Oramas, A. Ghodrati, and T. Tuytelaars, "Modeling video evolution for action recognition," in *2015 IEEE Conference on Computer Vision and Pattern Recognition (CVPR)*, Jun. 2015, pp. 5378–5387.
- [4] A. Shahroudy, J. Liu, T.-T. Ng, and G. Wang, "NTU RGB+D: A large scale dataset for 3D human activity analysis," pp. 1010–1019, Apr. 2016.
- [5] S. Yan, Y. Xiong, and D. Lin, "Spatial temporal graph convolutional networks for skeleton-based action recognition," in *AAAI*, 2018.
- [6] L. Shi, Y. Zhang, J. Cheng, and H. Lu, "Skeleton-Based action recognition with Multi-Stream adaptive graph convolutional networks," *IEEE Trans. Image Process.*, vol. PP, Oct. 2020.
- [7] M. Defferrard, X. Bresson, and P. Vandergheynst, "Convolutional neural networks on graphs with fast localized spectral filtering," in *Proceedings of the 30th International Conference on Neural Information Processing Systems*, ser. NIPS'16. Red Hook, NY, USA: Curran Associates Inc., Dec. 2016, pp. 3844–3852.
- [8] T. N. Kipf and M. Welling, "Semi-Supervised Classification with Graph Convolutional Networks," *International conference on learning representation*, p. 14, 2017.
- [9] B. Singh, T. K. Marks, M. Jones, O. Tuzel, and M. Shao, "A multi-stream bi-directional recurrent neural network for Fine-Grained action detection," in *2016 IEEE Conference on Computer Vision and Pattern Recognition (CVPR)*, Jun. 2016, pp. 1961–1970.

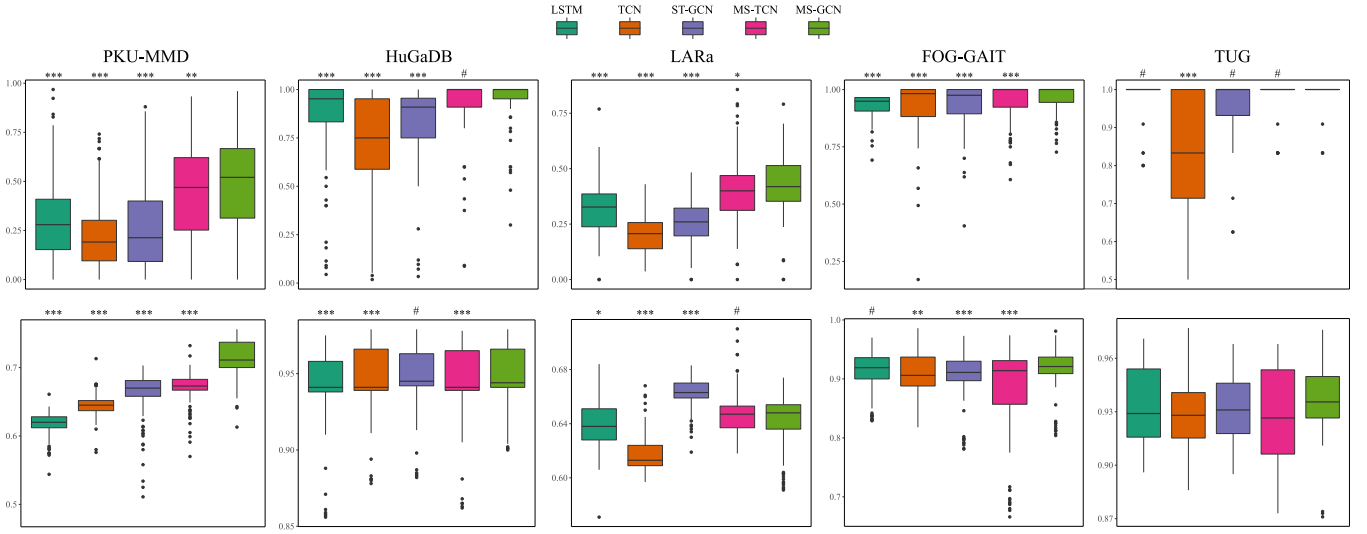


Fig. 7. Boxplots to visualize the spread in the segment-wise F1@50 (top row) and the sample-wise accuracy (bottom row) across trials per dataset. Significance levels were visualized as: $p \leq 0.01$ (***), $p \leq 0.05$ (**), $p \leq 0.1$ (*), and no significance (#). The Friedman test was significant at the $p \leq 0.01$ (***) level for all but the TUG dataset, for which the significance of the F1@50 was found to be $p \leq 0.05$ (**) and not significant for accuracy. The significance level of the post-hoc tests with respect to the MS-GCN model (corrected for multiple-comparisons) are visualized above their respective boxplot. No post-hoc tests were performed for the sample-wise accuracy of the TUG dataset since the Friedman test was not significant.

- [10] L. Sun, K. Jia, D.-Y. Yeung, and B. E. Shi, "Human action recognition using factorized Spatio-Temporal convolutional networks," in *2015 IEEE International Conference on Computer Vision (ICCV)*, Dec. 2015, pp. 4597–4605.
- [11] R. Yao, G. Lin, Q. Shi, and D. C. Ransinghe, "Efficient dense labelling of human activity sequences from wearables using fully convolutional networks," *Pattern Recognit.*, vol. 78, pp. 252–266, Jun. 2018.
- [12] C. Lea, M. D. Flynn, R. Vidal, A. Reiter, and G. D. Hager, "Temporal convolutional networks for action segmentation and detection," *Proceedings - 30th IEEE Conference on Computer Vision and Pattern Recognition, CVPR 2017*, vol. 2017-January, pp. 1003–1012, 2017.
- [13] Y. A. Farha and J. Gall, "Ms-tcn: Multi-stage temporal convolutional network for action segmentation," in *2019 IEEE/CVF Conference on Computer Vision and Pattern Recognition (CVPR)*, 2019, pp. 3570–3579.
- [14] B. Filtjens, P. Ginis, A. Nieuwboer, P. Slaets, and B. Vanrumste, "Automated freezing of gait assessment with marker-based motion capture and multi-stage graph convolutional neural networks approaches expert-level detection," *arXiv e-prints*, p. arXiv:2103.15449, Mar. 2021.
- [15] F. Yu and V. Koltun, "Multi-Scale context aggregation by dilated convolutions," *pre-print*, Nov. 2015.
- [16] I. Goodfellow, Y. Bengio, and A. Courville, *Deep Learning*. The MIT Press, 2016.
- [17] Y. Lecun, L. Bottou, Y. Bengio, and P. Haffner, "Gradient-based learning applied to document recognition," *Proc. IEEE*, vol. 86, no. 11, pp. 2278–2324, Nov. 1998.
- [18] S. Bai, J. Zico Kolter, and V. Koltun, "An empirical evaluation of generic convolutional and recurrent networks for sequence modeling," Mar. 2018.
- [19] A. Graves and J. Schmidhuber, "Framewise phoneme classification with bidirectional LSTM and other neural network architectures," *Neural Netw.*, vol. 18, no. 5-6, pp. 602–610, Jun. 2005.
- [20] B. Filtjens, A. Nieuwboer, N. D'cruz, J. Spildooren, P. Slaets, and B. Vanrumste, "A data-driven approach for detecting gait events during turning in people with parkinson's disease and freezing of gait," *Gait Posture*, vol. 80, pp. 130–136, Jul. 2020.
- [21] Y. Matsushita, D. T. Tran, H. Yamazoe, and J.-H. Lee, "Recent use of deep learning techniques in clinical applications based on gait: a survey," *Journal of Computational Design and Engineering*, vol. 8, no. 6, pp. 1499–1532, Oct. 2021.
- [22] N. Cheema, S. Hosseini, J. Sprenger, E. Herrmann, H. Du, K. Fischer, and P. Slusallek, "Dilated temporal Fully-Convolutional network for semantic segmentation of motion capture data," Jun. 2018.
- [23] S. Ioffe and C. Szegedy, "Batch normalization: Accelerating deep network training by reducing internal covariate shift," in *Proceedings of the 32nd International Conference on International Conference on Machine Learning (ICML)*, 2015.
- [24] M. Schuster and K. K. Paliwal, "Bidirectional recurrent neural networks," *Trans. Sig. Proc.*, vol. 45, no. 11, pp. 2673–2681, Nov. 1997.
- [25] Ł. Kidziński, S. Delp, and M. Schwartz, "Automatic real-time gait event detection in children using deep neural networks," *PLoS One*, vol. 14, no. 1, p. e0211466, Jan. 2019.
- [26] D. P. Kingma and J. Ba, "Adam: A method for stochastic optimization," *pre-print*, Dec. 2014.
- [27] C. Liu, Y. Hu, Y. Li, S. Song, and J. Liu, "PKU-MMD: A large scale benchmark for Skeleton-Based human action understanding," in *Proceedings of the Workshop on Visual Analysis in Smart and Connected Communities*, ser. VSCC '17. New York, NY, USA: Association for Computing Machinery, Oct. 2017, pp. 1–8.
- [28] R. Chereshevnev and A. Kertész-Farkas, "Hugadb: Human gait database for activity recognition from wearable inertial sensor networks," in *AIST*, 2017.
- [29] F. Niemann, C. Reining, F. Moya Rueda, N. R. Nair, J. A. Steffens, G. A. Fink, and M. Ten Hoppel, "LARa: Creating a dataset for human activity recognition in logistics using semantic attributes," *Sensors*, vol. 20, no. 15, Jul. 2020.
- [30] J. Spildooren, S. Vercruysse, K. Desloovere, W. Vandenberghe, E. Kerkhofs, and A. Nieuwboer, "Freezing of gait in parkinson's disease: the impact of dual-tasking and turning," *Mov. Disord.*, vol. 25, no. 15, pp. 2563–2570, Nov. 2010.
- [31] A. Nieuwboer, R. Dom, W. De Weerd, K. Desloovere, S. Fieuws, and E. Broens-Kaucsik, "Abnormalities of the spatiotemporal characteristics of gait at the onset of freezing in parkinson's disease," *Mov. Disord.*, vol. 16, no. 6, pp. 1066–1075, Nov. 2001.
- [32] J. D. Schaafsma, Y. Balash, T. Gurevich, A. L. Bartels, J. M. Hausdorff, and N. Giladi, "Characterization of freezing of gait subtypes and the response of each to levodopa in parkinson's disease," *Eur. J. Neurol.*, vol. 10, no. 4, pp. 391–398, Jul. 2003.
- [33] M. Gilat, "How to annotate freezing of gait from video: A standardized method using Open-Source software," *J. Parkinsons. Dis.*, vol. 9, no. 4, pp. 821–824, 2019.
- [34] A. Bowen, R. Wenman, J. Mickelborough, J. Foster, E. Hill, and R. Tallis, "Dual-task effects of talking while walking on velocity and balance following a stroke," *Age Ageing*, vol. 30, no. 4, pp. 319–323, Jul. 2001.
- [35] R. B. Davis, S. Öunpuu, D. Tyburski, and J. R. Gage, "A gait analysis data collection and reduction technique," *Hum. Mov. Sci.*, vol. 10, no. 5, pp. 575–587, Oct. 1991.
- [36] D. Podsiadlo and S. Richardson, "The timed 'up & go': a test of basic functional mobility for frail elderly persons," *J. Am. Geriatr. Soc.*, vol. 39, no. 2, pp. 142–148, Feb. 1991.

- [37] T. Li, J. Chen, C. Hu, Y. Ma, Z. Wu, W. Wan, Y. Huang, F. Jia, C. Gong, S. Wan, and L. Li, "Automatic timed Up-and-Go Sub-Task segmentation for parkinson's disease patients using Video-Based activity classification," *IEEE Trans. Neural Syst. Rehabil. Eng.*, vol. 26, no. 11, pp. 2189–2199, Nov. 2018.
- [38] P. Liang, W. H. Kwong, A. Sidarta, C. K. Yap, W. K. Tan, L. S. Lim, P. Y. Chan, C. W. K. Kuah, S. K. Wee, K. Chua, C. Quek, and W. T. Ang, "An asian-centric human movement database capturing activities of daily living," *Sci Data*, vol. 7, no. 1, p. 290, Sep. 2020.
- [39] A. Cappozzo, F. Catani, U. D. Croce, and A. Leardini, "Position and orientation in space of bones during movement: anatomical frame definition and determination," *Clin. Biomech.*, vol. 10, no. 4, pp. 171–178, Jun. 1995.
- [40] J. Demšar, "Statistical comparisons of classifiers over multiple data sets," *J. Mach. Learn. Res.*, vol. 7, no. 1, pp. 1–30, 2006.
- [41] S. García, A. Fernández, J. Luengo, and F. Herrera, "Advanced non-parametric tests for multiple comparisons in the design of experiments in computational intelligence and data mining: Experimental analysis of power," *Inf. Sci.*, vol. 180, no. 10, pp. 2044–2064, May 2010.
- [42] M. Friedman, "The use of ranks to avoid the assumption of normality implicit in the analysis of variance," *J. Am. Stat. Assoc.*, vol. 32, no. 200, pp. 675–701, Dec. 1937.
- [43] C. Borja and S. Guzman, "scmamp: Statistical comparison of multiple algorithms in multiple problems," *The R Journal*, vol. Accepted for publication, 2015.
- [44] R Core Team, *R: A Language and Environment for Statistical Computing*, R Foundation for Statistical Computing, Vienna, Austria, 2013. [Online]. Available: <http://www.R-project.org/>